

H α EMISSION AND THE DEPENDENCE OF THE CIRCUMGALACTIC COOL GAS FRACTION ON HALO MASS

HUANIAN ZHANG (张华年)¹, XIAOHU YANG (杨小虎)^{2,3}, DENNIS ZARITSKY¹, PETER BEHROOZI¹, AND JESSICA WERK⁴

Draft version November 7, 2019

ABSTRACT

We continue our empirical study of the emission line flux originating in the cool ($T \sim 10^4$ K) gas that populates the halos of galaxies and their environments. Specifically, we present results obtained for a sample of nearly half a million individual galaxies, groups, and clusters of galaxies, intersected by more than two million SDSS lines of sight at projected separations of up to a quarter of the virial radius. Adopting simple power law relationships between the circumgalactic (CGM) cool gas fraction and either the halo or stellar mass, we present expressions for the CGM cool gas fraction as a function of either halo or stellar mass, $f_{\text{cool}}(M_h) = (0.25_{-0.06}^{+0.07}) \times (M_h/10^{12} M_\odot)^{(-0.39_{-0.07}^{+0.06})}$ or $f_{\text{cool}}(M_*) = (0.28_{-0.06}^{+0.07}) \times (M_*/10^{10.0} M_\odot)^{(-0.33 \pm 0.06)}$. Where we can compare, our results are consistent with previous constraints from absorption line studies, our own previous emission line work, and simulations. The cool gas can be the dominant baryonic CGM component, comprising a fraction as high as $> 90\%$ of halo gaseous baryons, in low mass halos, $M_h \sim 10^{10.5} M_\odot$, and a minor fraction, $< 5\%$, in groups and clusters, $M_h > 10^{14} M_\odot$.

Subject headings: galaxies: kinematics and dynamics, structure, halos, intergalactic medium

1. INTRODUCTION

Galaxies are surrounded by extended and diffuse gas, referred to as the circumgalactic medium (CGM), which is a critical but incompletely understood part of galactic ecosystems (Tumlinson, Peebles & Werk 2017). Previous studies (e.g., Behroozi, Conroy & Wechsler 2010; McGaugh et al. 2010) concluded that only $\sim 20\%$ of all the baryons apportioned to a given halo have been converted into stars for L^* galaxies. The corresponding fractions are even lower for sub- L^* and super- L^* galaxies, typically only $\sim 5\text{--}10\%$. The common inference is that the majority of the original baryons in a given halo remain in the halo and comprise the CGM.

The CGM is a multi-phase medium with rich dynamics and complex ionization states (Bregman 2007; Werk et al. 2014). It provides the fuel for subsequent star formation activities (Spitzer 1956) and serves as the depository for galactic recycling and feedback (Tumlinson, Peebles & Werk 2017). Empirical constraints on the nature of the CGM have come primarily from the study of absorption lines in the spectra of bright background objects (e.g. Steidel et al. 2010; Ménard et al. 2011; Bordoloi et al. 2011; Zhu & Ménard 2013a,b; Werk et al. 2014, 2016; Croft et al. 2016, 2018; Prochaska et al. 2017; Cai et al. 2017; Lan & Mo 2018; Joshi et al. 2018). Unfortunately, absorption line studies are limited by the requirement of a sufficiently bright background source and so typically probe a single sight line through each of a limited set of halos. As such, a valuable complement to these studies is the detection and study of emission line flux from the CGM, which will eventually provide spatially resolved measurements of the CGM of individual galaxies and, by doing so, help resolve modeling degeneracies and provide

novel constraints.

Zhang et al. (2016) presented the first detection of the emission line flux, H α +N[II], from low redshift, normal galaxies extending out to ~ 100 kpc projected radius. This measurement could only be achieved with existing data by stacking a sample of over 7 million lines of sight from the Sloan Digital Sky Survey (SDSS DR12; Alam et al. 2015). Building on that first result, we have applied the technique to characterize the nature of the emission and the CGM in low redshift galaxies and their environments (Zhang et al. 2016; Zhang, Zaritsky & Behroozi 2018; Zhang et al. 2018, 2019, hereafter, Papers I, II, III, and IV).

In those studies, our focus was on the nature of line emission from the halos of “normal” galaxies. As such, we purposefully limited the range of galaxy masses and sizes considered. Now, we expand the range of halo masses considered as much as possible to characterize the cool gas halo component as a function of halo mass. The virial temperature of the halo gas can be as low as 10^{4-5} K for small halos with mass $\lesssim 10^{11} M_\odot$ and as high as 10^{6-7} K for large halos with mass $\gtrsim 10^{13} M_\odot$. Given this large range of virial temperatures, one naturally expects a strong trend in the fraction of the CGM that is in the cool gas phase ($T \sim 10^4$ K) as a function of mass.

Our aim here is to build on existing evidence from absorption line studies and detailed theoretical modeling for such a trend (Werk et al. 2014; Ford et al. 2014; Suresh et al. 2017) and refine the quantitative description of the trend using stacked emission line measurements. Throughout the paper we adopt a Λ CDM cosmology with parameters $\Omega_m = 0.3$, $\Omega_\Lambda = 0.7$, $\Omega_k = 0$ and the dimensionless Hubble constant $h = 0.7$ (cf. Riess et al. 2018; Planck Collaboration et al. 2018).

2. DATA ANALYSIS

2.1. The Parent Sample

We begin by describing the set of systems about which we will measure the emission flux from the surrounding cool gas. Because we are expanding the halo mass range explored relative to our previous studies, our systems now span classification from individual galaxies, to galaxy groups, and in-

¹ Steward Observatory, University of Arizona, Tucson, AZ 85719, USA; fantasyzhn@email.arizona.edu

² Department of Astronomy, School of Physics and Astronomy, Shanghai JiaoTong University, Shanghai, 200240, China

³ Tsung-Dao Lee Institute, and Shanghai Key Laboratory for Particle Physics and Cosmology, Shanghai Jiao Tong University Shanghai, 200240, China

⁴ Department of Astronomy, University of Washington, Seattle, WA 98195, USA

nally to galaxy clusters. For simplicity, we will refer to all systems with multiple luminous galaxies as galaxy groups, even those that would generally be referred to as galaxy clusters. In this regard, we utilize an existing “group” catalog (Yang et al. 2012, hereafter Y12)⁵, which is based on the work of Yang et al. (2007).

We briefly describe how that catalog was constructed for completeness. Y12 selected galaxies with redshifts in the range $0.01 \leq z \leq 0.20$, and a redshift completeness⁶ $C_z > 0.7$ from the main galaxy sample of the New York University Value-Added Galaxy Catalog (NYU-VAGC Blanton et al. 2005) for the SDSS DR7 (Abazajian et al. 2009). This selection results in a sample of 639,359 galaxies scattered over 7748 square degrees. From this galaxy sample, a galaxy group catalog was constructed using an adaptive halo-based group finder (see Yang et al. 2007, 2012, for details). For each identified system, whether it is a single galaxy or a multiple galaxy system, the dark matter halo mass, M_h , is estimated using the rank of the system’s total stellar mass, M_{stellar} , which is defined to be the sum of the stellar mass of all members with $^{0.1}M_r - 5 \log h \leq -19.5$, and a ranked halo mass function.

Meanwhile, we take into account the redshift completeness limit of the groups, and adopt the halo mass function for a given cosmology to determine the halo mass of the most massive halo expected within this volume, the second most massive, and so on. We then assign the group with the largest stellar mass the most massive halo and work our way down the rankings. The details of such a halo mass estimation algorithm is described in detail in §3.5 of Y07. As Y07 show, the estimated masses recover the true halo masses with a $1\text{-}\sigma$ deviation of ~ 0.3 dex for L^* galaxies, although the scatter at the small mass end is unknown (Allen, Behroozi & Ma 2018), and are more reliable than those based on the velocity dispersion of group members (Yang et al. 2005; Weinmann et al. 2006; Berlind et al. 2006). For those groups where all the member galaxies are fainter than $^{0.1}M_r - 5 \log h = -19.5$, the halo masses are estimated according to the stellar to halo mass relation for central galaxies obtained in Y12.

The resulting catalog, constructed from 639,324 galaxies, contains 472,416 identified systems, of which 23,735 are groups with three or more galaxy members, 44,470 are binaries, and the remaining 404,211 are isolated galaxies. A critical property of the catalog is that systems with only one member are not satellite galaxies associated with larger galaxies or groups, they are independent, parent halos. The isolated galaxies may have satellites that are fainter than the spectroscopic limit or companions that may have been missed due to spectroscopic incompleteness above the magnitude limit. The mean and median derived halo masses for $N = 3$ groups are $10^{12.86}$ and $10^{13.04} M_\odot$, respectively. About 10% (42,198) of the isolated galaxies are assigned halo masses greater than that of the mean $N = 3$ group. For the halo mass range where individual and multi-galaxy systems overlap, the resulting H α fluxes that we measure as described below are within the 1σ uncertainties whether we include or exclude the massive individual galaxies. We detect no difference in the CGM emission properties of isolated and group galaxies in this overlapping

⁵ see <http://gax.sjtu.edu.cn/data/Group.html>

⁶ Because of the fiber-collision effects, some neighboring galaxies in the SDSS observations do not have spectroscopic redshifts. This effect becomes increasingly important in dense environments, so we set the redshift completeness criteria.

mass range and provide quantitative support for this claim in §3.

The halo masses for the cataloged objects range from $10^{10.7} M_\odot$, for systems with only one member galaxy, to $10^{15.0} M_\odot$, for systems with > 500 member galaxies. We display the distribution of the halo masses for the cataloged systems in Figure 1. The dashed red lines indicates the boundaries of four different mass bins that we define. We select these bins to correspond broadly to halos similar in mass to that of 1) the Large Magellanic Cloud ($\sim 10^{11.40} M_\odot$; Peñarrubia et al. 2016), 2) the Milky Way ($\sim 10^{12} M_\odot$; Zaritsky et al. 1989), 3) massive galaxies like M 87 ($\sim 10^{13} M_\odot$; Zhu et al. 2014b), and 4) everything else from poor groups to the most massive clusters ($\gtrsim 0.5 \times 10^{14} M_\odot$; Zabludoff & Mulchaey 1998). At the same time, we are trying to balance the number of halos in each mass bin as much as possible. The average halo mass of objects in each of the four mass bins are $10^{11.27}$, $10^{11.97}$, $10^{12.72}$ and $10^{13.75} M_\odot$.

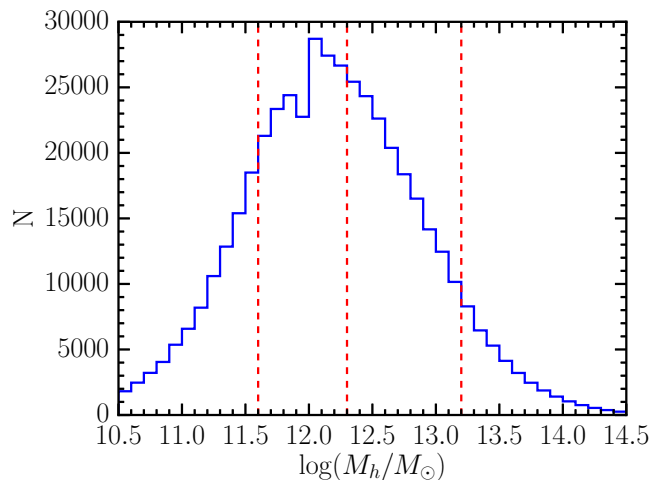


FIG. 1.— The distribution of halo masses in the catalog. The dashed vertical lines show the boundaries we set between the four mass bins we use in our analysis.

2.2. The Stacking Analysis

In expanding our analysis from a limited sample of galaxies in Papers I-IV to the wider variety of systems considered now, we introduce several complications. First, while the center for an individual galaxy is fairly straightforward to identify, the center of a group or cluster is more ambiguous. Second, with a sample of fairly similar galaxies, we could stack our results in terms of physical projected radius. For our current sample, we cannot stack on physical projected radius because a fixed radius probes quite different physical regimes in different halos. Third, in this work we will be measuring composite emission line profiles. For individual galaxies, we probe gas in their halos when we restrict ourselves to < 50 kpc projected separation (Zhang et al. 2016), but for groups we are measuring the combination of the cool gas from the parent and satellite halos. As such, our measurements are of the total cool gas in these halos, whether it is physically associated with the parent or satellites. Our previous work (Zhang et al. 2019) suggests that emission from satellite halos in dense environments is suppressed, so our measurement may indeed primarily reflect the gas associated with the parent, but this

interpretation cannot be established within this analysis.

In general, we follow the approach developed in Papers I-IV. We obtain galaxy spectra from the Sloan Digital Sky Survey Data Releases (Alam et al. 2015, SDSS DR12) projected within 1 Mpc of the targets described above (Yang et al. 2012). The outer 1 Mpc separation limit is sufficiently large to satisfy the rescaling that we describe further below. To avoid contamination from emission arising in the luminous centers of satellites or other nearby galaxies, we exclude SDSS lines of sight that targeted galaxies whose redshift are within 0.05 of our defined target. For each remaining spectrum, we fit and subtract a 10th order polynomial to a 300 Å wide section at the rest wavelength, in the target reference frame, of H α to remove the continuum. **Various tests of the procedure, including the injection and accurate recovery of emission lines of known flux, are described in detail in Zhang et al. (2016).** Unlike in previous papers, where we measured both H α and [NII], here we focus solely on H α to simplify the modeling and interpretation.

2.2.1. Centering

Defining the sample of spectra and stacking in terms of projected separation requires a definition of the “center” of each target. For isolated galaxies, that is unambiguous, but for multiple galaxy systems there are at least two options. One can define the center to correspond to the position of the brightest group galaxy (BGG) or to the luminosity weighted center (LWC) of all the identified member galaxies. We will explore both approaches, but focus on the results using the LWC, which results in centers that are consistently defined across systems that do and do not have a clearly dominant galaxy.

We find that the choice of center is not critical in our analysis. The center as defined in these two ways tends to differ at a level of between 1 and 10 kpc for systems with 2 or more members. Given that we do not use the inner 10 kpc of the profile in our analysis, to avoid contamination from emission from the central galaxy, the resulting differences in profiles are expected to be relatively minor. We do, nevertheless, compare our results using both methods even though we present the quantitative results from the LWC approach in figures and modeling results. We find that the results we present are insensitive to the choice of centering.

2.2.2. Rescaling

Comparing the properties of a set of systems with highly disparate masses and sizes requires some care. Specifically, we need to compare measurements at similar, representative projected radii and over appropriate velocity windows. We do not favor comparing results at physical radii. For example, a projected radius of 25 kpc corresponds to a halo position for a sub- L^* galaxy but is likely to be within the BGG of our most massive clusters. Instead, we will compare results at scaled radii. Likewise, we need to take care how we integrate along the line of sight. Integrating over a velocity window of width 400 km sec $^{-1}$ will include all of the bound gas in a low mass galaxy but only a limited fraction of the gas in a massive cluster.

We choose to measure the emission line fluxes in bins of scaled projected radius (r_s), where we scale the physical projected radius (r_p) in terms of the virial radius ($r_s \equiv r_p/R_{180}$). We estimate the virial radius ($\equiv R_{180}$) using the following equation from Yang et al. (2007):

$$R_{180} = 780 h^{-1} \text{kpc} \left(\frac{M_h}{\Omega_m 10^{14} h^{-1} M_\odot} \right)^{1/3} (1+z)^{-1} \quad (1)$$

where R_{180} is the radius within which the mean halo density is 180 times the current critical density. We will measure the flux for $0.05 \leq r_s \leq 0.25$, which corresponds to a range of 10 to 50 kpc for an $\sim L^*$ galaxy and matches our previous work using fixed physical radii. For $M_h > 10^{14} M_\odot$, the virial radius is $\gtrsim 2$ Mpc and then the r_s range corresponds to physical projected radii of 100 to 500 kpc.

We measure the emission flux within a prescribed velocity window relative to the target in each individual spectra that probes the halo and then combine these measurements. Because M_h spans a few orders of magnitude, we need to vary the size of the velocity window. For targets in each of the four mass bins, we scale the window roughly to the characteristic virial velocity of targets in the bin, adopting windows of ± 100 km s $^{-1}$, ± 215 km s $^{-1}$, ± 330 km s $^{-1}$, and ± 450 km s $^{-1}$. At the ends of the virial velocity distribution we have too large a window for our least massive objects and too small a window for our most massive due to the long tails of the mass distribution (Figure 1).

This limiting of the velocity window scaling at low and high velocities does not affect our results. At the low velocity end our window is larger than that we would have if we continued our scaling downward. Only in highly crowded environments might an overly large velocity window allow flux from neighbors to contaminate the measurement. However, these targets are almost certainly isolated, since any neighbor is likely to be more massive and this target would then not have been categorized as isolated. To confirm that this windowing of the lowest mass galaxies is not affecting our results, we redo our measurement of the H α flux in the lowest mass bin excluding all systems with $M_{\text{halo}} < 10^{11} M_\odot$. The measured flux drops from 0.011 ± 0.004 to 0.0082 ± 0.0044 , but the new value is statistically consistent with the original one. This test demonstrates that the effect of a large window on these lowest mass systems is not resulting in a systematic error that is larger than the statistical errors. At the high end of halo mass range, our window is not as large as it should be and we could be losing flux. We had to limit the size of the window to avoid contaminating the H α measurement with [N II] emission. **This criteria limits the maximum velocity difference between the central galaxy and H α CGM emission to < 450 km sec $^{-1}$, which is below the virial velocity for the more massive systems.** To test for the choice of window size on the measured H α fluxes in the largest M_h bin, we now measure the flux in a velocity window where the blue end of the spectral window is defined by the full characteristic virial velocity and at the upper by 0 relative velocity. We would expect such a choice of velocity window to result in a measurement of half of the total flux. We can do this as a test because the [N II] line that is blueward of H α is much weaker than the redder one and is rarely detected in our stacks (Zhang et al. 2016). **By then doubling the flux in this blueward-extended velocity window (our lower velocity limit is set to -1350 km s $^{-1}$), we have an estimate of what we would measure across the full window if we did not have to limit its extent in either direction.** We find that these new measurement is -0.00030 ± 0.0013 , to be compared to the original measurement of 0.00080 ± 0.0011 for the smaller r_s bin, and is -0.00006 ± 0.00066 , to be compared to 0.00039 ± 0.00037 , for the larger r_s bin. **The test results** are statistically consistent with our previous measurements. We conclude that although not ideal, our truncated velocity window is not introducing systematic uncertainties that are larger than our internal statistical uncertainties in our

largest M_h bins.

We also appeal for justification of our choice to absorption line studies that find that the CGM gas is typically found at velocities well below the escape speed. Werk et al. (2013) and Tumlinson et al. (2013) find that most of the absorption is within 150 km sec^{-1} of the galaxy’s systemic velocity even when the escape speed was estimated to be 300 km s^{-1} . Nevertheless, one might expect some gas to be escaping, particularly in the lower mass systems (e.g., Bordoloi et al. 2014). Tripp et al. (2011) find a few examples of absorption line systems offset in velocity by more than the escape speed. This gas could be interpreted as escaping or perhaps it is associated with other galaxies, as we find gas at large projected radii to be Zhang, Zaritsky & Behroozi (2018). Even if it is escaping gas, it is not evident that we would want to be including it in our measurement if our aim is to quantify the gas reservoir for future star formation.

3. RESULTS

We present stacked measurements of the $\text{H}\alpha$ fluxes in two r_s bins (the inner bin spans $0.05 < r_s < 0.11$ and the outer bin spans $0.11 < r_s < 0.25$) as a function of M_h and M_* in Table 1⁷. We do not extend the radial range beyond $r_s = 0.25$ because the $\text{H}\alpha$ flux beyond $r_s = 0.25$ for $\sim L^*$ galaxies becomes increasingly dominated by the contribution from associated halos, not the target galaxy itself (Zhang, Zaritsky & Behroozi 2018). In figures and tables we present the median emission line fluxes and the associated uncertainties, estimated using a jackknife method. Specifically, we randomly select half of the individual spectra, calculate the mean emission line flux and repeat the process 1000 times to establish the distribution of measurements from which we quote the values corresponding to the 16.5 and 83.5 percentiles as the lower and upper uncertainties, respectively. Returning to the question of whether the emission flux is similar for similarly massive single or multiple galaxy systems that we first discussed in §2.1, we note that if we remove the isolated galaxies from the bin with $\langle M_h \rangle = 10^{12.72} M_\odot$, the new values of the fluxes in the inner and outer radius bins are 0.0024 ± 0.012 and 0.0012 ± 0.0005 , respectively, and nearly indistinguishable from the values in Table 1.

3.1. Emission Fluxes as a Function of System Mass

In Figure 2 we present the $\text{H}\alpha$ emission fluxes at two different scaled radii as a function of halo mass **and in Figure 3 as a function of stellar mass**. We see a systemic decline in the flux at both radii as the masses increase. **Even had the flux remained flat as a function of mass, the fraction of the baryonic reservoir that this represent would be declining rapidly because the halo mass is increasing by a factor of ~ 300 across the plotted mass ranges.** These trends suggest a strong inverse relationship between the fraction of the CGM in the cool component vs. halo mass.

3.2. Modeling the Cool Gas Fraction vs Halo Mass

The results in Figure 2 imply that the cool gas fraction, C_f , declines strongly with M_h , but they do not directly tell us what that dependence is. To place constraints on that relation we turn to a straightforward modeling tool that we employed previously in Papers II and IV. The methodology is

⁷ The conversion factor to units between the values we present, $10^{-17} \text{ erg cm}^{-2} \text{ s}^{-1} \text{ \AA}^{-1}$ and those used commonly in the literature to describe diffuse line emission, $\text{erg cm}^{-2} \text{ s}^{-1} \text{ arcsec}^{-2}$, is 1.7.

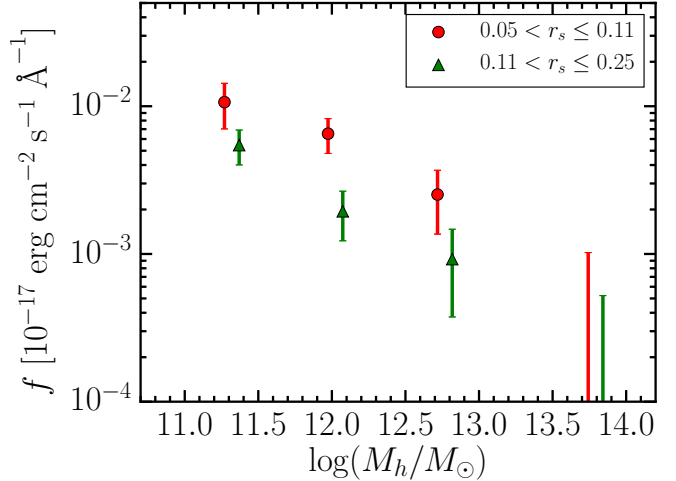


FIG. 2.— The $\text{H}\alpha$ emission fluxes at two values of r_s for four different halo mass ranges. For visualization, we apply slight horizontal offsets to the two samples although they have the same halo mass.

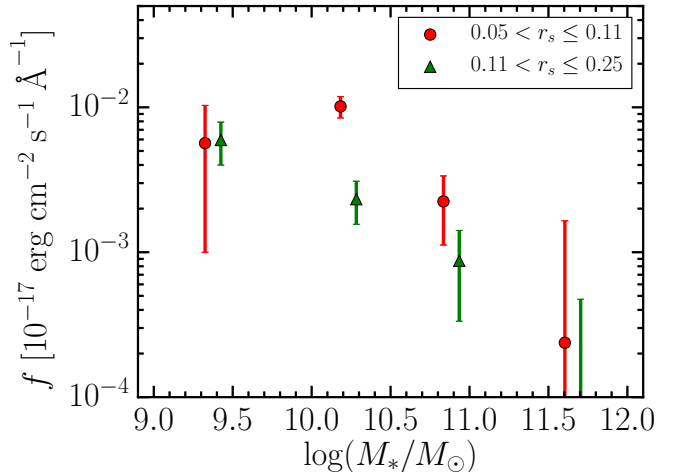


FIG. 3.— The $\text{H}\alpha$ emission fluxes at two values of r_s for four different stellar mass ranges. For visualization, we apply slight horizontal offsets to the two samples although they have the same stellar mass.

based on the UniverseMachine architecture (Behroozi et al. 2018) where standard Λ CDM dark matter halos within a cosmological volume are populated with luminous galaxies in a manner to match available observational constraints. We then apply a hypothesized behavior for the dependence of the cool CGM gas fraction on halo mass and produce mock observations where the selection function is matched closely to the real observations. The parameters of that hypothesized behavior are constrained by producing a model that can reproduce the observations.

Some assumptions are needed to populate the modeled halos with the gas that produces the $\text{H}\alpha$ emission. First, we adopt an analytic description for the gas density profile within a dark matter halo derived for gas in an NFW potential (Navarro, Frenk & White 1996, 1997) in hydrostatic equilibrium (Capelo, Natarajan & Coppi 2010). Second, we need to adopt a certain range of temperatures for the cool gas component that we are modeling. In previous papers, we drew on a rough estimation of the temperature as 10^4 K . This choice

TABLE 1
THE EMISSION FLUXES FOR H α AS A FUNCTION OF RADIUS AND HALO MASS/STELLAR MASS^a

r_s	Halo Mass			
	$10^{11.27} M_\odot$	$10^{11.97} M_\odot$	$10^{12.72} M_\odot$	$10^{13.75} M_\odot$
0.08	0.011 ± 0.004	0.0065 ± 0.0018	0.0025 ± 0.0012	-0.0003 ± 0.0013
0.2	0.0055 ± 0.0015	0.0019 ± 0.0007	0.0010 ± 0.0005	$-5 \times 10^{-5} \pm 0.0006$
r_s	Stellar Mass			
	$10^{9.33} M_\odot$	$10^{10.18} M_\odot$	$10^{10.84} M_\odot$	$10^{11.60} M_\odot$
0.08	0.0057 ± 0.0046	0.010 ± 0.002	0.0022 ± 0.0010	0.0002 ± 0.0014
0.2	0.0059 ± 0.0021	0.0023 ± 0.0008	0.00087 ± 0.00050	-0.0001 ± 0.0006

^a Fluxes in units of $10^{-17} \text{ erg cm}^{-2} \text{ s}^{-1} \text{ \AA}^{-1}$

is supported by studies finding that the temperature distribution is bimodal, with one peak around $\sim 10^6$ K and another centered at $\sim 10^4$ K (Haider et al. 2016; Cui et al. 2019). The cool gas temperature, T , is an important parameter as it sets the recombination rate, $\beta_{\text{H}\alpha}$,

$$\beta_{\text{H}\alpha} = 10^{-13} \frac{2.274 T^{-0.659}}{1 + 1.939 T^{0.574}} \quad (2)$$

(Pequignot, Petitjean & Boisson 1991). While the assumption of a single characteristic temperature, with some allowed scatter, is defensible when modeling a narrow range of systems, it becomes more questionable as one explores the large range of systems we are dealing with here. We will discuss this issue further below.

Once the shape of the radial density profile and temperature of the cool gas are defined, we need to specify the fraction of CGM that is in this phase. Our cool gas fraction, f_{cool} ⁸, refers, as in our previous papers, to the fraction of CGM baryons that are in the $T \sim 10^4$ K phase. We calculate this fraction starting with the assumption that each halo contains its fair share of baryons, the cosmological baryon fraction or 16% (Planck Collaboration et al. 2018), that 80% of those baryons are in the form of CGM (as inferred from the deficit between the identified stellar plus gaseous mass and halo mass; Behroozi, Conroy & Wechsler 2010), and that 75% of those, by mass, are hydrogen (ionized or neutral, **adopting the standard universal hydrogen mass fraction**). The cool gas fraction is then the percentage of the hydrogen that must be at $\sim 10^4$ K to generate the observed H α flux. We model the behavior of f_{cool} with halo mass as a power law,

$$f_{\text{cool}}(M_h) = a \times \left(\frac{M_h}{10^{12} M_\odot} \right)^b \quad (3)$$

where M_h is the halo mass, (a, b) are fitting parameters. We adopt a scatter of 0.3 dex to the halo mass, **which is consistent with Y07 although the scatter at the small mass end**

⁸ Here we denote cool gas fraction as f_{cool} instead of C_f , because C_f in CGM absorption measurements refers to recovering fraction.

is unknown (Allen, Behroozi & Ma 2018), to simulate the halo mass uncertainty resulting from the conversion of stellar mass to halo mass. To be specific, we estimate the cool gas fraction using Eq. 3 with the true halo mass, and then we add scatter to the halo mass when placing each system into its corresponding mass bins.

We perform a Bayesian analysis to derive confidence intervals on each of the model parameters, (a, b, T) . The prior on a we take from our previous work, where the $f_{\text{cool}} \sim 0.3$ for $\sim L_*$ galaxies, so we allow $0 < a < 0.5$. The prior on b is informed by the previous determination, based on absorption line observations, that the cool gas fraction decreases as the galaxy mass increases (Ford et al. 2014). So we adopt that the slope b must be negative. Finally, we adopt a large range of allowed temperatures. In all cases, we adopt uniform priors within the allowed ranges. To summarize, our priors are:

$$\begin{aligned} 0 < a < 0.5, \quad -1 < b < 0, \\ 3000 < T < 30000, \quad a \times 0.025^b < 1 \end{aligned} \quad (4)$$

The additional condition that we apply, $a \times 0.025^b < 1$, is imposed so that the cool gas fraction of any halo is less than one. The posterior distribution, $p(\Theta|\text{data})$, for the parameters based on the data is described as follows:

$$p(\Theta|\text{data}) = \frac{p(\Theta) \cdot \Pi p(\text{data}|\Theta)}{p(\text{data})} \quad (5)$$

where Θ is the parameter space $\Theta = (a, b, T)$, $p(\Theta)$ is the prior distribution described in Eq. 4, $p(\text{data}|\Theta)$ is the likelihood of the data, and $p(\text{data})$ is the marginal probability for the data.

We define the likelihood of obtaining the data given a specific model using the difference between the actual and model data, $\exp[-0.5 \times (\text{actual} - \text{model})^2 / \sigma^2]$, where σ is the observational uncertainty. We fit the data for the four mass bins at the two values of r_s . We use the software package called “emcee” (Foreman-Mackey et al. 2013), which implements a Markov chain Monte Carlo sampling of the likelihoods across parameter space to calculate the posterior distribution. *emcee* is a *Python* implementation of the affine-invariant ensemble

sampling approach suggested by Goodman & Weare (2010). It utilizes an ensemble of N walkers, and it will evolve each for a certain number of steps. We initialize each walker (total 500 walkers in our simulation) by randomly sampling from our prior distributions, and evolving each walker for 1500 steps. We discard the first 250 steps since it takes a certain number of steps (~ 100 in this study) for the results to become stable.

In Figure 4 we present the posterior distributions of the model parameters $\Theta = (a, b, T)$, as well as the median value and the one σ confidence level (based on the 16th and 84th percentiles), and the correlations between them. The preferred value of a , $0.25^{+0.07}_{-0.06}$, indicates that the cool gas fraction for \sim Milky Way size galaxy with halo mass $10^{12} M_{\odot}$ is $25^{+7}_{-6}\%$. The preferred value of b , $-0.39^{+0.06}_{-0.07}$, confirms that the cool gas fraction decreases significantly with increasing halo mass. The median value of temperature with one σ confidence level is 7200^{+5000}_{-2800} K, consistent with both our previous estimation (Zhang et al. 2016) and the bimodal distribution of temperature with one peak centered on 10^4 K (Haider et al. 2016; Cui et al. 2019). **This is not only the most likely fit, but is in absolute terms a good fit, with a $\chi^2_{\nu} = 0.87$, which can only be rejected with $< 0.5\%$ confidence.**

In the analogous model for the cool gas fraction as a function of stellar mass, M_* , is scaled by $10^{10} M_{\odot}$ and the relation is $f_{\text{cool}}(M_*) = a \times (\frac{M_*}{10^{10} M_{\odot}})^b$. The preferred value of a , $0.28^{+0.07}_{-0.06}$, indicates that the cool gas fraction for \sim a galaxy with stellar mass $10^{10.0} M_{\odot}$ is $28^{+7}_{-6}\%$. The preferred value of b , and T are -0.33 ± 0.06 , and 9500^{+7100}_{-3600} K, respectively.

3.3. Comparison to Previous Results

We show the posterior distribution for the cool gas fraction of the CGM, within projected radii of $0.05 < r_s < 0.25$, as a function of halo mass in Figure 5. If we assume that this fraction is relatively independent of the radius over which it is measured, then we can easily compare the results to those from other studies and simulations. We compare first to our own previous estimates (Paper II) of 0.34 ± 0.081 for low mass halos ($M_h \approx 10^{11.7} M_{\odot}$) and 0.26 ± 0.05 for high mass halos ($M_h \approx 10^{12.4} M_{\odot}$). These values are consistent with our current results.

Next, we compare our results to estimates from various published studies in Figure 5. We plot cool gas fraction measurements derived from absorption line observations by Werk et al. (2014). They present a range of f_{cool} for gas at $T \sim 10^4$ K from 0.25 to 0.45. We adopt $f_{\text{cool}} = 0.35 \pm 0.1$ for halos of mass $10^{12.2} M_{\odot}$ to represent their result, **which is slightly more than one σ away from our prediction** (0.21 ± 0.06). Prochaska et al. (2017) report a higher value of f_{cool} based on absorption line measurements for similar mass galaxies ($M_h \sim 10^{12.15} M_{\odot}$) of 0.48 ± 0.22 , **which is also slightly more than one σ away from our prediction** (0.22 ± 0.07). Zhu et al. (2014a) find that the cool gas traced by Mg II in the halos of luminous red galaxies with mass $\sim 10^{13.5} M_{\odot}$ is between 10^{10} and $10^{11} M_{\odot}$, assuming 0.1 solar abundance. This measurement corresponds to cool gas fractions of 0.0025 to 0.025.

Given the current large uncertainties, **we consider our results to be statistically consistent with previous observational results. Nevertheless, one might argue that there is a slight tension at $\sim L^*$ mass scales between the absorption line results and ours given the slightly larger than 1 σ differ-**

ences, where the absorption line measurements indicate larger f_{cool} . This tension may reflect the difference in approaches, in which we actively account for contributions from neighboring galaxies both by limiting the projected radius and including the contribution of neighboring galaxies in our modeling.

Comparing to results from simulations is a bit more complicated. We were able to extract values for the cool gas fraction from both Ford et al. (2014) and Suresh et al. (2017) but these values correspond to all gas with temperature $< 10^5$ K. As such, these values may somewhat overestimate their predicted fractions of gas at $T \sim 10^4$ K. With this caveat in mind, we still find excellent agreement both in the normalization and in the behavior of f_{cool} with M_h . There are a number of other simulations of the CGM (e.g., Oppenheimer et al. 2016), but it is often difficult to extract quantities that are directly comparable to our observations. We encourage future simulators to present predicted line emission “images” of the CGM.

3.4. Caveats

There are a number of complicating factors in our measurements of cool gas fraction of the CGM and the interpretation of our empirical results.

3.4.1. The f_{cool} and T Model Degeneracy

Because the emission flux depends on both the cool gas fraction f_{cool} and temperature T (Eqs. 2 and 3), those two parameters are somewhat degenerate in our modeling. So far, however, we have not allowed T to vary with M_h so there is a concern that some of the derived variation of f_{cool} on M_h could rather be due to a variation of T with M_h .

One option is to allow both f_{cool} and T to vary with M_h in our modeling. Unfortunately, we have only a few data points to fit and as such the resulting constraints are poor. Nevertheless, we explore the alternative modeling scenario where both f_{cool} and T have a power law dependence on M_h . The resulting fit has f_{cool} with $a = 0.25 \pm 0.08$ and $b = -0.37^{+0.06}_{-0.07}$, which is almost indistinguishable from the previous estimation, while **for the associated power law model for T it results in $a = 1.63^{+2.72}_{-1.10} \times 10^4$ and $b = 1.52^{+0.36}_{-0.87}$** . T is poorly constrained. We conclude that our initial adoption of a single value for T is not significantly affecting the behavior we are inferring for f_{cool} as a function of M_h .

3.4.2. Clumpiness

We assume a smooth gas distribution characterized by an equilibrium gas distribution within an NFW potential. The adoption of both the equilibrium model and the smooth density distribution are questionable. Further guidance on these topics from detailed simulations is an urgent need. However, the agreement in the overall observed radial emission profile (Zhang, Zaritsky & Behroozi 2018) suggests that the density profile is not likely to be grossly different from what we have adopted. Even so, local changes in gas density are problematic as the emission depends on density squared and can affect the overall normalization of the profile.

In our models, we only change the fraction of gas in the cool component, f_{cool} . However, an additional degree of freedom that should be considered is the clumpiness of this cool gas. We have discussed this degree of freedom previously (Zhang, Zaritsky & Behroozi 2018). While we have no additional insights into modeling this behavior, we note that on the basis of our comparison to absorption line results and simulations (Figure 5) we would not expect clumpiness

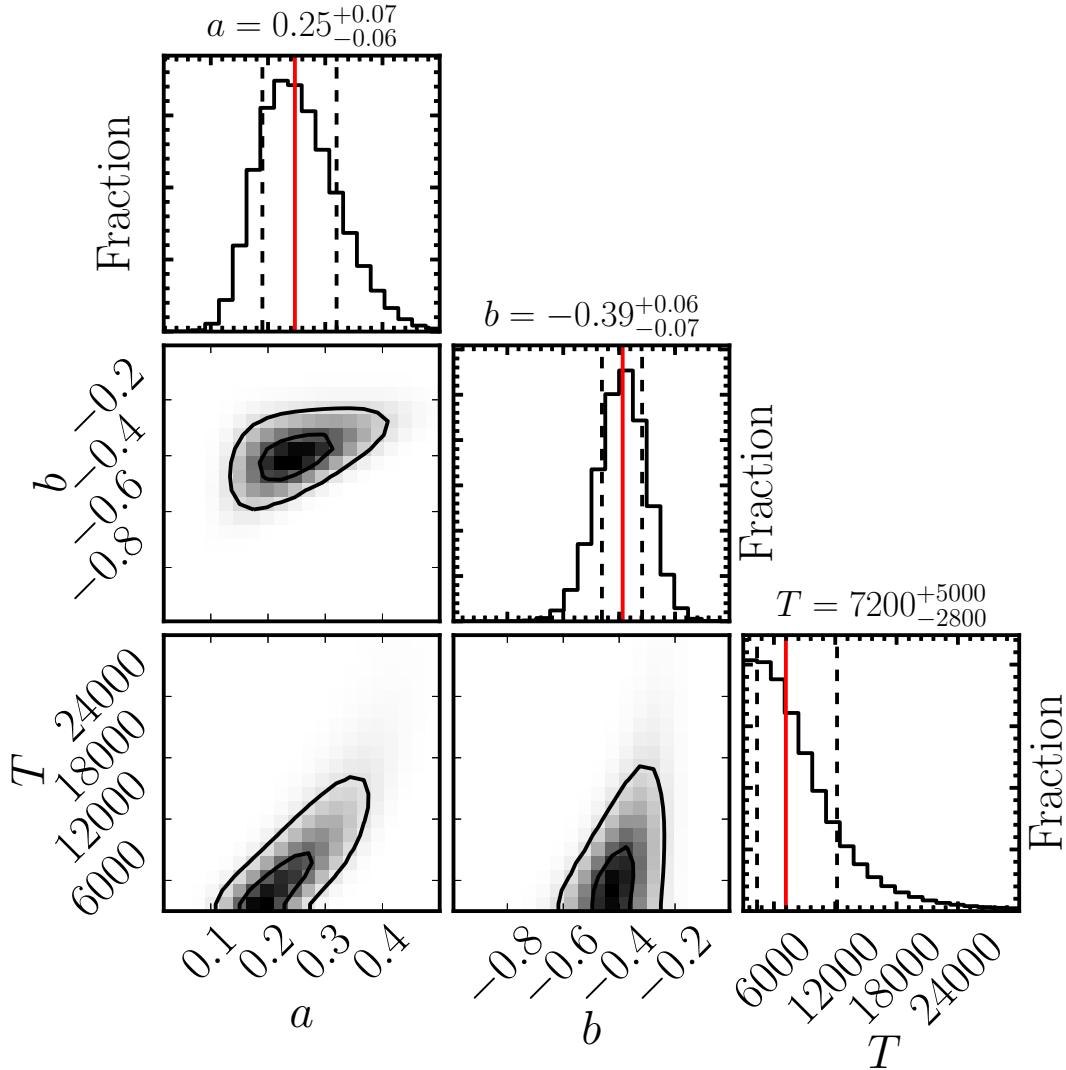


FIG. 4.— Posterior probability distributions for model parameters a , b , and T , and the correlations between them. We display the median value (red vertical line), lower error estimated by the 16% value and higher error estimated by the 84% value (dashed black vertical line) for the model parameters a , b , and T . The two contours in the correlation plot represent 68% (small one) and 95% (big one) confidence levels.

to significantly alter our derived values of f_{cool} . Clumpiness would in general lower the required values of f_{cool} and as such might result in somewhat better agreement with the Ford et al. (2014) results, although both the observational results of Werk et al. (2014) and the simulations of Suresh et al. (2017) suggest that f_{cool} is not much lower than what we have found in our reference model.

The degree of clumpiness could vary as a function of halo mass (see Fielding et al. 2017, for an example of varying CGM morphology that depends on mass), which would affect the distribution we show in Figure 5. Clumping might, in fact, help bring the f_{cool} values down for the lowest mass systems.

4. SUMMARY

We present measurements of the $\text{H}\alpha$ emission line flux as a function of halo or stellar mass, M_h and M_* , respectively, at two different scaled radius for systems spanning $10^{10.7} < M_h < 10^{15} M_\odot$ and $10^{8.7} < M_* < 10^{12.5}$. The flux at both radii drops as both M_h or M_* increase, indicating a strong inverse relationship between the cool gas

fraction of the CGM, f_{cool} and both M_h and M_* . Using a highly simplified model of cool gas in halos, we quantify the behavior of f_{cool} with M_h and M_* : $f_{\text{cool}}(M_h) = (0.25^{+0.07}_{-0.06}) \times (M_h/10^{12} M_\odot)^{(-0.39^{+0.06}_{-0.07})}$ and $f_{\text{cool}}(M_*) = (0.28^{+0.07}_{-0.06}) \times (M_*/10^{10.0} M_\odot)^{(-0.33 \pm 0.06)}$. Our prediction for the cool gas fraction is as high as 90% for the smallest halos we probe, $26^{+7}_{-6}\%$ for a Milky Way like galaxy, and only a few percent for the most massive clusters.

These results are consistent with results from previous absorption line studies (0.35 ± 0.1 for $M_h \sim 10^{12.2} M_\odot$; Werk et al. 2014) and simulations (Ford et al. 2014; Suresh et al. 2017), where comparison is possible.

The quantitative results we present are tentative in the sense that they rely on highly simplified models. There are a number of complications that we neglected, principally the clumpiness of the gas, deviations in the gas distribution from the hot gas in thermodynamical equilibrium, and the assumption of a constant cool gas fraction across radii. The agreement in the derived f_{cool} 's with absorption line studies and simulations suggests that our simplifications do not

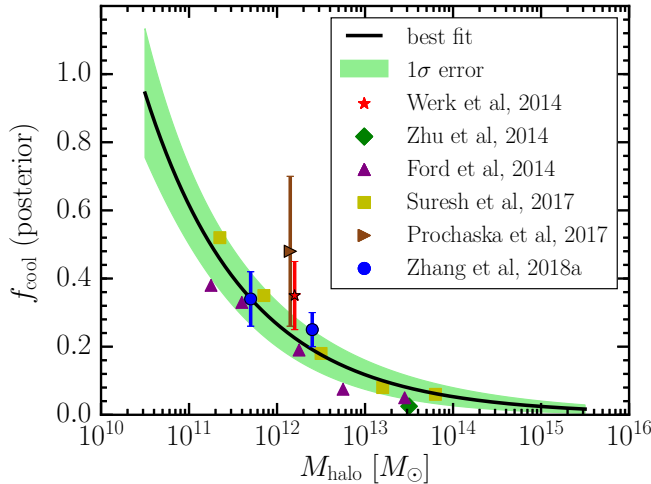


FIG. 5.— The posterior cool gas fraction as a function of the halo mass. The shaded region indicates the 1σ uncertainty estimated from the entire MCMC sample. The data points from both Ford et al. (2014) and Suresh et al. (2017) are corresponding to gas with temperature $< 10^5$ K.

grossly affect our inferences, but our measurements warrant detailed comparison to results from more realistic CGM models. Stacking is providing a range of new constraints on the cool CGM (Zhang et al. 2016; Zhang, Zaritsky & Behroozi 2018; Zhang et al. 2018, 2019), with the potential to provide even more both from the further analysis of SDSS spectra and from the future analysis of DESI (Levi et al. 2013) data. We strongly encourage simulators to provide predicted CGM properties projected onto this observational space and to identify what observations will best distinguish between models.

5. ACKNOWLEDGMENTS

DZ and HZ acknowledge financial support from NSF grant AST-1713841. This work is supported by the 973 Program (Nos. 2015CB857002) and national science foundation of China (grant Nos. 11833005, 11890692, 11621303). We also thank the support of the Key Laboratory for Particle Physics, Astrophysics and Cosmology, Ministry of Education. The authors gratefully acknowledge the SDSS III team for providing a valuable resource to the community. Funding for SDSS-III has been provided by the Alfred P. Sloan Foundation, the Participating I institutions, the National Science Foundation, and the U.S. Department of Energy Office of Science. The SDSS-III web site is <http://www.sdss3.org/>.

SDSS-III is managed by the Astrophysical Research Consortium for the Participating Institutions of the SDSS-III Collaboration including the University of Arizona, the Brazilian Participation Group, Brookhaven National Laboratory, Carnegie Mellon University, University of Florida, the French Participation Group, the German Participation Group, Harvard University, the Instituto de Astrofísica de Canarias, the Michigan State/Notre Dame/JINA Participation Group, Johns Hopkins University, Lawrence Berkeley National Laboratory, Max Planck Institute for Astrophysics, Max Planck Institute for Extraterrestrial Physics, New Mexico State University, New York University, Ohio State University, Pennsylvania State University, University of Portsmouth, Princeton University, the Spanish Participation Group, University of Tokyo, University of Utah, Vanderbilt University, University of Virginia, University of Washington, and Yale University.

REFERENCES

- Abazajian K. N., et al., 2009, *ApJS*, 182, 543
Alam S., Albareti F. D., Allende Prieto C., Anders F., Anderson S. F., Anderton T., Andrews B. H., et al., 2015, *ApJS*, 219, 12
Allen M., Behroozi P., Ma C.-P., 2018, arXiv e-prints, arXiv:1812.05733
Behroozi P., Wechsler R., Hearin A., Conroy C., 2018, ArXiv e-prints
Behroozi P. S., Conroy C., Wechsler R. H., 2010, *ApJ*, 717, 379
Berlind A. A. et al., 2006, *ApJS*, 167, 1
Blanton M. R., et al., 2005, *AJ*, 129, 2562
Bordoloi R., Lilly S. J., Knobel C., Bolzonella M., Kampczyk P., Carollo C. M., et al., 2011, *ApJ*, 743, 10
Bordoloi R. et al., 2014, *ApJ*, 796, 136
Bregman J. N., 2007, *ARA&A*, 45, 221
Cai Z. et al., 2017, *ApJ*, 837, 71
Capelo P. R., Natarajan P., Coppi P. S., 2010, *MNRAS*, 407, 1148
Croft R. A. C., Miralda-Escudé J., Zheng Z., Blomqvist M., Pieri M., 2018, *MNRAS*
Croft R. A. C., Miralda-Escudé J., Zheng Z., Bolton A., Dawson K. S., Peterson J. B., York D. G., et al., 2016, *MNRAS*, 457, 3541
Cui W. et al., 2019, *MNRAS*, 485, 2367
Fielding D., Quataert E., McCourt M., Thompson T. A., 2017, *MNRAS*, 466, 3810
Ford A. B., Davé R., Oppenheimer B. D., Katz N., Kollmeier J. A., Thompson R., Weinberg D. H., 2014, *MNRAS*, 444, 1260
Foreman-Mackey D., Hogg D. W., Lang D., Goodman J., 2013, *PASP*, 125, 306
Goodman J., Weare J., 2010, *Communications in Applied Mathematics and Computational Science*, Vol. 5, No. 1, p. 65-80, 2010, 5, 65
Haider M., Steinhauser D., Vogelsberger M., Genel S., Springel V., Torrey P., Hernquist L., 2016, *MNRAS*, 457, 3024
Joshi R., Srianand R., Petitjean P., Noterdaeme P., 2018, *MNRAS*, 476, 210
Lan T.-W., Mo H., 2018, ArXiv 1806.05786
Levi M. et al., 2013, arXiv e-prints, arXiv:1308.0847
McGaugh S. S., Schombert J. M., de Blok W. J. G., Zagursky M. J., 2010, *ApJ*, 708, L14
Ménard B., Wild V., Nestor D., Quider A., Zibetti S., Rao S., Turnshek D., 2011, *MNRAS*, 417, 801
Navarro J. F., Frenk C. S., White S. D. M., 1996, *ApJ*, 462, 563
Navarro J. F., Frenk C. S., White S. D. M., 1997, *ApJ*, 490, 493
Oppenheimer B. D. et al., 2016, *MNRAS*, 460, 2157
Peñarrubia J., Gómez F. A., Besla G., Erkal D., Ma Y.-Z., 2016, *MNRAS*, 456, L54
Pequignot D., Petitjean P., Boisson C., 1991, *A&A*, 251, 680
Planck Collaboration et al., 2018, arXiv e-prints, arXiv:1807.06205
Prochaska J. X., Werk J. K., Worseck G., Tripp T. M., Tumlinson J., et al., 2017, *ApJ*, 837, 169
Riess A. G. et al., 2018, *ApJ*, 861, 126
Spitzer, Jr. L., 1956, *ApJ*, 124, 20
Steidel C. C., Erb D. K., Shapley A. E., Pettini M., Reddy N., Bogosavljević M., Rudie G. C., Rakic O., 2010, *ApJ*, 717, 289
Suresh J., Rubin K. H. R., Kannan R., Werk J. K., Hernquist L., Vogelsberger M., 2017, *MNRAS*, 465, 2966
Tripp T. M. et al., 2011, *Science*, 334, 952
Tumlinson J., Peebles M. S., Werk J. K., 2017, *ARA&A*, 55, 389
Tumlinson J. et al., 2013, *ApJ*, 777, 59
Weinmann S. M., van den Bosch F. C., Yang X., Mo H. J., 2006, *MNRAS*, 366, 2
Werk J. K., Prochaska J. X., Cantalupo S., Fox A. J., Oppenheimer B., Tumlinson J., Tripp T. M., et al., 2016, *ApJ*, 833, 54
Werk J. K., Prochaska J. X., Thom C., Tumlinson J., Tripp T. M., O’Meara J. M., Peebles M. S., 2013, *ApJS*, 204, 17
Werk J. K., Prochaska J. X., Tumlinson J., Peebles M. S., Tripp T. M., Fox A. J., et al., 2014, *ApJ*, 792, 8
Yang X., Mo H. J., van den Bosch F. C., Jing Y. P., 2005, *MNRAS*, 356, 1293
Yang X., Mo H. J., van den Bosch F. C., Pasquali A., Li C., Barden M., 2007, *ApJ*, 671, 153
Yang X., Mo H. J., van den Bosch F. C., Zhang Y., Han J., 2012, *ApJ*, 752, 41

Zabludoff A. I., Mulchaey J. S., 1998, ApJ, 496, 39
Zaritsky D., Olszewski E. W., Schommer R. A., Peterson R. C., Aaronson
M., 1989, ApJ, 345, 759
Zhang H., Zaritsky D., Behroozi P., 2018, ApJ, 861, 34
Zhang H., Zaritsky D., Behroozi P., Werk J., 2019, ApJ in press
Zhang H., Zaritsky D., Werk J., Behroozi P., 2018, ApJ, 866, L4

Zhang H., Zaritsky D., Zhu G., Ménard B., Hogg D. W., 2016, ApJ, 833, 276
Zhu G., Ménard B., 2013a, ApJ, 773, 16
Zhu G., Ménard B., 2013b, ApJ, 770, 130
Zhu G. et al., 2014a, MNRAS, 439, 3139
Zhu L. et al., 2014b, ApJ, 792, 59